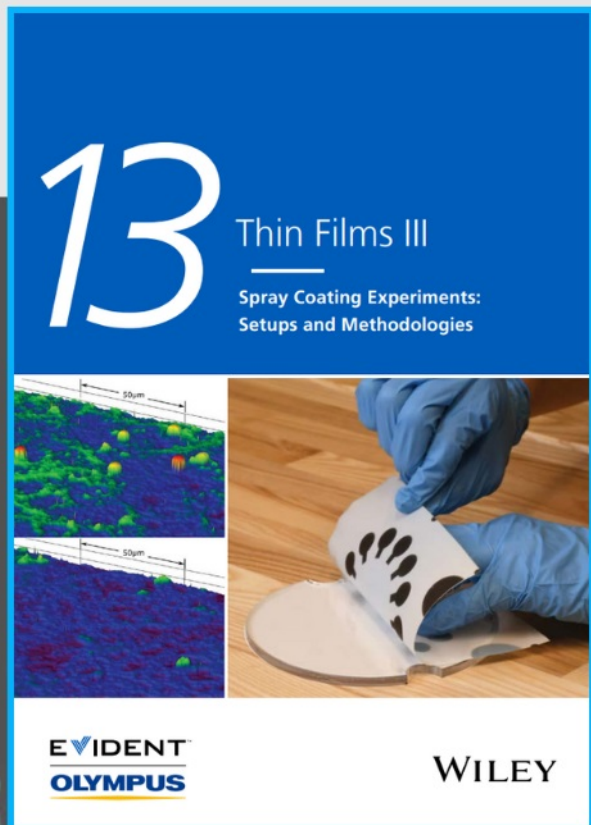




Spray Coating Experiments: Setups and Methodologies

**The latest eBook from
Advanced Optical Metrology.
Download for free.**



Spray Coating Experiments: Setups and Methodologies, is the third in our Thin Films eBook series. This publication provides an introduction to spray coating, three article digests from Wiley Online Library and the latest news about Evident's Image of the Year Award 2022.

Wiley in collaboration with Evident, are committed to bridging the gap between fundamental research and industrial applications in the field of optical metrology. We strive to do this by collecting and organizing existing information, making it more accessible and useful for researchers and practitioners alike.

EVIDENT
OLYMPUS

WILEY

RuO₂ Supercapacitor Enables Flexible, Safe, and Efficient Optoelectronic Neural Interface

Onuralp Karatum, Erdost Yildiz, Humeyra Nur Kaleli, Afsun Sahin, Burak Ulgut, and Sedat Nizamoglu*

Optoelectronic biointerfaces offer a wireless and nongenetic neurostimulation pathway with high spatiotemporal resolution. Fabrication of low-cost and flexible optoelectronic biointerfaces that have high photogenerated charge injection densities and clinically usable cell stimulation mechanism is critical for rendering this technology useful for ubiquitous biomedical applications. Here, supercapacitor technology is combined with flexible organic optoelectronics by integrating RuO₂ into a donor–acceptor photovoltaic device architecture that facilitates efficient and safe photostimulation of neurons. Remarkably, high interfacial capacitance of RuO₂ resulting from reversible redox reactions leads to more than an order-of-magnitude increase in the safe stimulation mechanism of capacitive charge transfer. The RuO₂-enhanced photoelectrical response activates voltage-gated sodium channels of hippocampal neurons and elicits repetitive, low-light intensity, and high-success rate firing of action potentials. Double-layer capacitance together with RuO₂-induced reversible faradaic reactions provide a safe stimulation pathway, which is verified via intracellular oxidative stress measurements. All-solution-processed RuO₂-based biointerfaces are flexible, biocompatible, and robust under harsh aging conditions, showing great promise for building safe and highly light-sensitive next-generation neural interfaces.


O. Karatum, S. Nizamoglu
Department of Electrical and Electronics Engineering
Koc University
Istanbul 34450, Turkey
E-mail: snizamoglu@ku.edu.tr

E. Yildiz, H. N. Kaleli, A. Sahin
Research Center for Translational Medicine
Koc University
Istanbul 34450, Turkey

A. Sahin
Department of Ophthalmology
Medical School
Koc University
Istanbul 34450, Turkey

B. Ulgut
Department of Chemistry
Bilkent University
Ankara 06800, Turkey

S. Nizamoglu
Department of Biomedical Science and Engineering
Koc University
Istanbul 34450, Turkey

 The ORCID identification number(s) for the author(s) of this article can be found under <https://doi.org/10.1002/adfm.202109365>.

DOI: 10.1002/adfm.202109365

1. Introduction

Bioelectronics uses electrical stimulation of neurons to treat a wide variety of diseases such as hearing loss, Parkinson's disease, epileptic seizures, and depression without drug injection into the body.^[1] In bioelectronic devices, electrical signals, which are converted to ionic currents at the abiotic–biotic interfaces, are generally carried to the targeted tissues via wires. Instead, light offers a wireless stimulation trigger^[2] enabling minimally invasive implantation of the optoelectronic devices and operation at high spatiotemporal resolution.^[3] Silicon-based optoelectronic devices are successfully used for photostimulation of retina,^[4] but the low absorption coefficient of silicon due to its indirect bandgap necessitates thicker devices, which adds to the overall rigidity, volume, and weight of the devices.^[5] Alternatively, organic optoelectronics shows high promise for next-generation neural interfaces due to the high absorbance

and unique solution processability of organic semiconductors, which together enable low-cost and configurable device fabrication, lower thickness, and flexibility.^[6]

For organic optoelectronic neural interfaces, stimulation mechanism and efficiency of conversion of light to ionic currents are important to ensure safe operation without damaging tissues and to enhance the dynamic range of the devices, respectively. Since irreversible faradaic reactions can change the pH and deteriorate homeostasis of the cellular environment, operation using double-layer capacitance or reversible faradaic reactions is critical for safe stimulation.^[7] In fact, supercapacitors, which show high promise for energy storage applications, are based on fast and reversible reduction–oxidation (redox) reactions at the electrode–electrolyte interface, which yield notably large interfacial capacitance values.^[8] This phenomenon can be fundamentally used for photostimulation of neurons by organic neural interfaces.^[9] Among pseudocapacitive materials (e.g., PEDOT:PSS^[10]), RuO₂ is one of the most studied supercapacitor materials as it has the highest specific capacitance ($\approx 1000 \text{ F g}^{-1}$).^[11] Although different ruthenium complexes (e.g., Ru²⁺/Ru³⁺) have been previously used as anticancer agents,^[12] supercapacitor RuO₂ has attracted little attention for biomedicine^[13] and bioelectronics,^[14] and has not been explored for organic optoelectronic neural interfaces yet.

Here, we demonstrate that RuO₂ supercapacitor significantly boosts photogenerated charge injection densities over 20-fold in biological fluid of artificial cerebrospinal fluid (aCSF) in comparison with the control devices without RuO₂. It enables safe, repetitive, and low-light intensity photostimulation of hippocampal neurons below 1 mW mm⁻². More interestingly, we developed an all-solution-processed fabrication (on a flexible substrate) of organic optoelectronic neural interfaces by sensitive incorporation of RuO₂ via electrochemical deposition that allowed high-level control and optimization of charge injection density. The results point out that RuO₂ is a powerful material option for flexible optoelectronic neural interfaces and its electrochemical integration enables biocompatible, robust, and highly light-sensitive devices for future retinal implants.

2. Results

The solution-processed fabrication of the optoelectronic neural interface started with the sequential spin-coating of ZnO nanoparticles (NPs) and P3HT:PCBM bulk heterojunction (BHJ) thin films on fluorine-doped tin oxide (FTO)/indium tin oxide (ITO) substrates (Figure 1a). During these steps, a part of the substrate was covered with a mask to prevent the deposition of ZnO NPs and P3HT:PCBM BHJ to the area where RuO₂ return electrode will be formed. Then, after removal of the mask, RuO₂ layer was coated on the back electrode (FTO/ITO) via cyclic voltammetric deposition.^[15]

We investigated the structural properties of RuO₂ films having different number of electrodeposition cycles (5, 15, 25, 40, 60). The atomic force microscopy (AFM; Figure S1, Supporting Information) revealed surface morphology of RuO₂ coatings, which have root-mean-square (RMS) surface roughness of 15.8, 15.6, 18.4, 22.9, and 23.1 nm for 5-, 15-, 25-, 40-, and 60-cycle RuO₂ coatings, respectively. Considering the maximum diffusion length of protons in RuO₂ (≈20 nm), those roughness values are at desirable levels for facilitating ion transportation during fast redox reactions.^[16] X-ray photoelectron spectroscopy (XPS) analysis of Ru 3d_{5/2} spectrum (Figure S2, Supporting Information) indicates a high amount of Ru(IV) species due to the peak at 281.4 eV corresponding to RuO₂·xH₂O,^[17] which are involved in the reversible redox reactions of Ru⁴⁺/Ru³⁺ couple.^[18] Scanning electron microscopy (SEM) images of RuO₂ coatings show a porous film morphology with progressively narrowing pore sizes as the deposition cycle increases (Figure 1b; for SEM images of all five coatings, see Figure S3, Supporting Information). Advantageously, porous coatings of capacitive materials offer potentially high electrochemical surface area/geometrical surface area (ESA/GSA) ratio for high charge capacities, which can be optimized by controlling the thickness through deposition cycles (Figure 1c).^[19]

To assess the effectiveness of RuO₂ coatings under physiological conditions, we performed cyclic voltammetry (CV) and electrochemical impedance spectroscopy (EIS) in aCSF. Figure 1d displays the cyclic voltammograms of RuO₂ coatings after different amounts of deposition cycles. The symmetric and quasi-rectangular shapes of cyclic voltammograms of RuO₂ coatings reveal the capacitive behavior of films through reversible redox reactions. Based on cyclic voltammograms,

we calculated the capacitance and cathodic charge storage capacity (CSC_c), which is commonly used as a characterization parameter for stimulation electrodes. Capacitance and CSC_c follows a similar sigmoidal-like trend (Figure 1e). For the five-cycle RuO₂ deposition, whose thickness is ≈10 nm (Figure 1c), the CSC_c is 2.5 ± 0.5 mC cm⁻² (mean ± s.d.), which is similar to the reported value for ≈10 nm SIROF coating.^[19] For 60-cycle RuO₂ (≈110 nm), CSC_c reaches to 19.8 ± 1.7 mC cm⁻² (mean ± SD), which is on the same order with sputtering.^[14a] In the range where our biointerfaces operate (0–0.5 V) the capacitive charge-transfer mechanism is evident (Figure 1f).

The long-term stability of 60-cycle RuO₂ deposition, which has the highest capacitance and CSC_c, was evaluated by subjecting the RuO₂ coating to 10 000 continuous CV cycles (Figure 1g). The current density due to the interfacial capacitance of RuO₂ is well-preserved after 10 000 cycle, which denotes its excellent long-term stability. Finally, Figure 1h shows the Nyquist plots of RuO₂ coatings obtained by EIS analysis. We fitted the high-frequency region with a resistance (R) and the low-frequency region with a resistance–constant phase element (R–Q) (Figure S4, Supporting Information). In the high-frequency region, 5-, 15-, and 25-cycle RuO₂ coatings exhibited similar resistances, while 40- and 60-cycle RuO₂ coatings display increased resistances possibly due to their higher film thickness and narrower pore sizes (Table S1, Supporting Information). In the low-frequency region, imaginary impedance was gradually decreasing as the cycle number increased (Table S1, Supporting Information), indicating higher capacitance values for thicker films as we observed in CV measurements. Even though the capacitance value from the CV followed the trend of the number of deposition cycles, the capacitance measured using EIS showed 25 cycles as an outlier, which is probably because of the increased resistance and thus lower porosity.

High CSC and capacitance of RuO₂ indicate its potential for achieving improved charge injection levels for the optoelectronic neural interface. To experimentally test that, we studied the effect of RuO₂ on the photoresponse of a control device. In our device architecture, ZnO/P3HT:PCBM photovoltaic heterostructure serves as the photocurrent-generating electrode. P3HT:PCBM BHJ absorbs the impinging light and afterward electron–hole pairs are dissociated at the donor–acceptor interface. Free electrons are transferred toward ITO through ZnO NPs. ZnO layer serves as the hole blocker due to its valence band energy level and electron transporter owing to its high electron mobility.^[20] The device design consists of ZnO/P3HT:PCBM layer over 1 cm² area of the ITO-coated substrate and electrodeposited RuO₂ film over the remaining 0.5 cm² area of the same substrate (Figure 2a). The control devices are bare ITO as the return electrode without RuO₂ coating.

We analyzed the photoelectrical performance of the control and RuO₂ biointerfaces by comparing their charge-injection performances in a wireless, free-standing measurement setup (Figure 2b). Devices were placed in aCSF and injected charge was measured in voltage-clamp mode with a patch pipette that is positioned close to the biointerface surface (<5 μm). This measurement configuration demonstrates the ability of biointerfaces to perturb the local electric equilibrium at the device–electrolyte interface, revealing the potential of the biointerface to stimulate

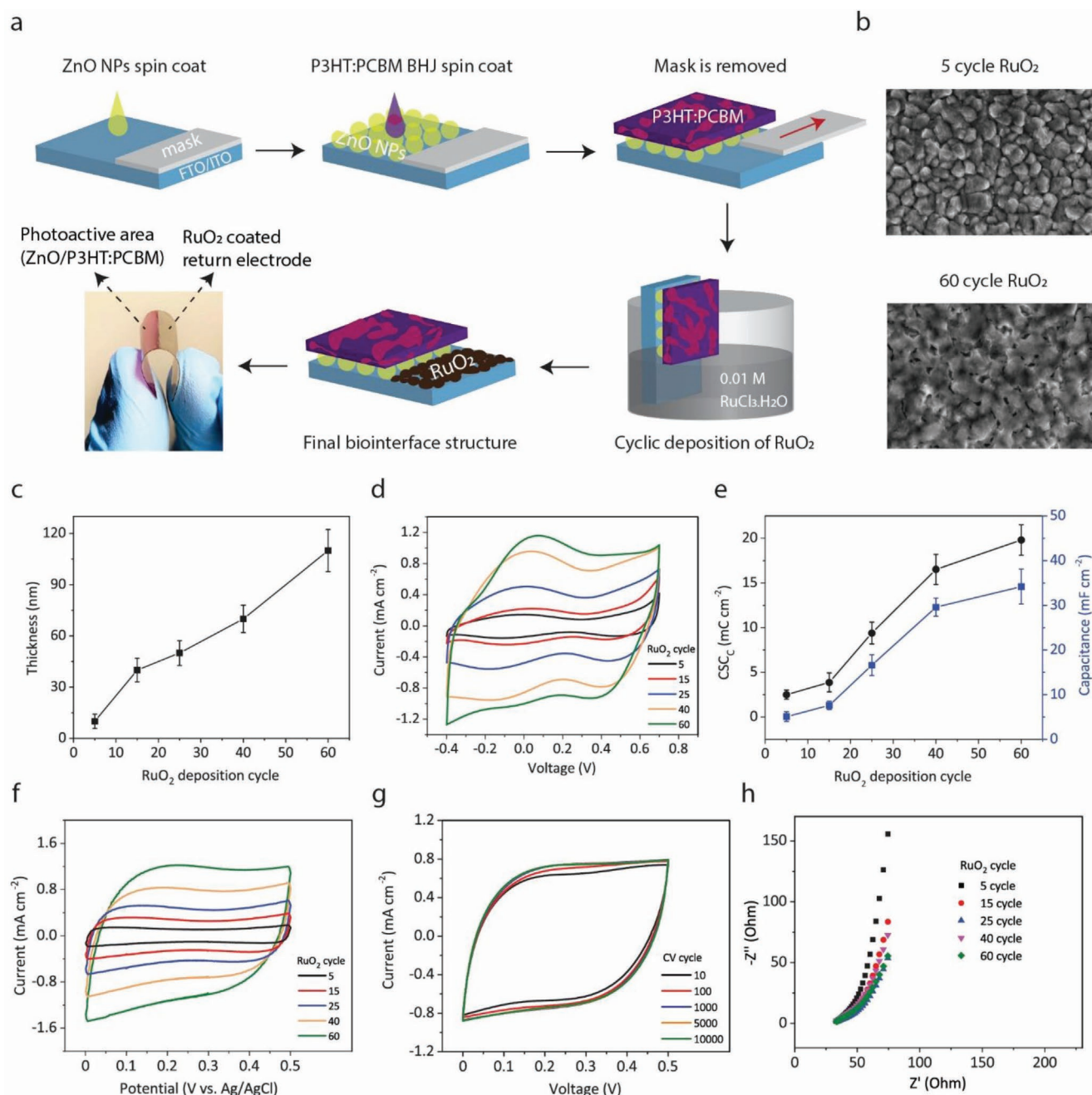


Figure 1. Fabrication of RuO₂-based optoelectronic biointerfaces, and structural and electrochemical characterization of RuO₂ coatings. a) Sequential fabrication of RuO₂-based biointerfaces with a photograph of the produced flexible device. b) Surface SEM images of 5-cycle and 60-cycle RuO₂ coatings. c) Thickness of RuO₂ coatings as a function of deposition cycle. d) Cyclic voltammograms of RuO₂ coatings from −0.4 to 0.7 V range, which is within the water electrolysis window.^[14a] Scan rate is 50 mV s^{−1}. e) Cathodic charge storage capacity (CSC_c) and capacitance of RuO₂ coatings extracted from cyclic voltammograms shown in (d). f) Cyclic voltammograms of RuO₂ coatings in the operation range of the biointerfaces (0–0.5 V). Scan rate is 50 mV s^{−1}. g) Long-term cyclic stability of 60-cycle RuO₂ coating measured over 10 000 cycles in 0–0.5 V. Scan rate is 100 mV s^{−1}. h) Electrochemical impedance measurement of RuO₂ coatings within the frequency range of 1–10 000 Hz.

neurons. The photoresponse of the control devices was characterized by an initial capacitive peak triggered by light onset and a second peak with a smaller magnitude taking place with the end of illumination (Figure 2c). The capacitive onset peak decays rapidly to its ground level, meaning no significant capacitive current is flowing under steady illumination condition

because of the double-layer capacitance with minimal Faradaic reactions under steady photovoltage.^[21] This considerably limits the amount of injected charge required for effective stimulation of neurons.

After RuO₂ deposition, the reversible surface redox processes induced by the coating lead to a remarkable amount

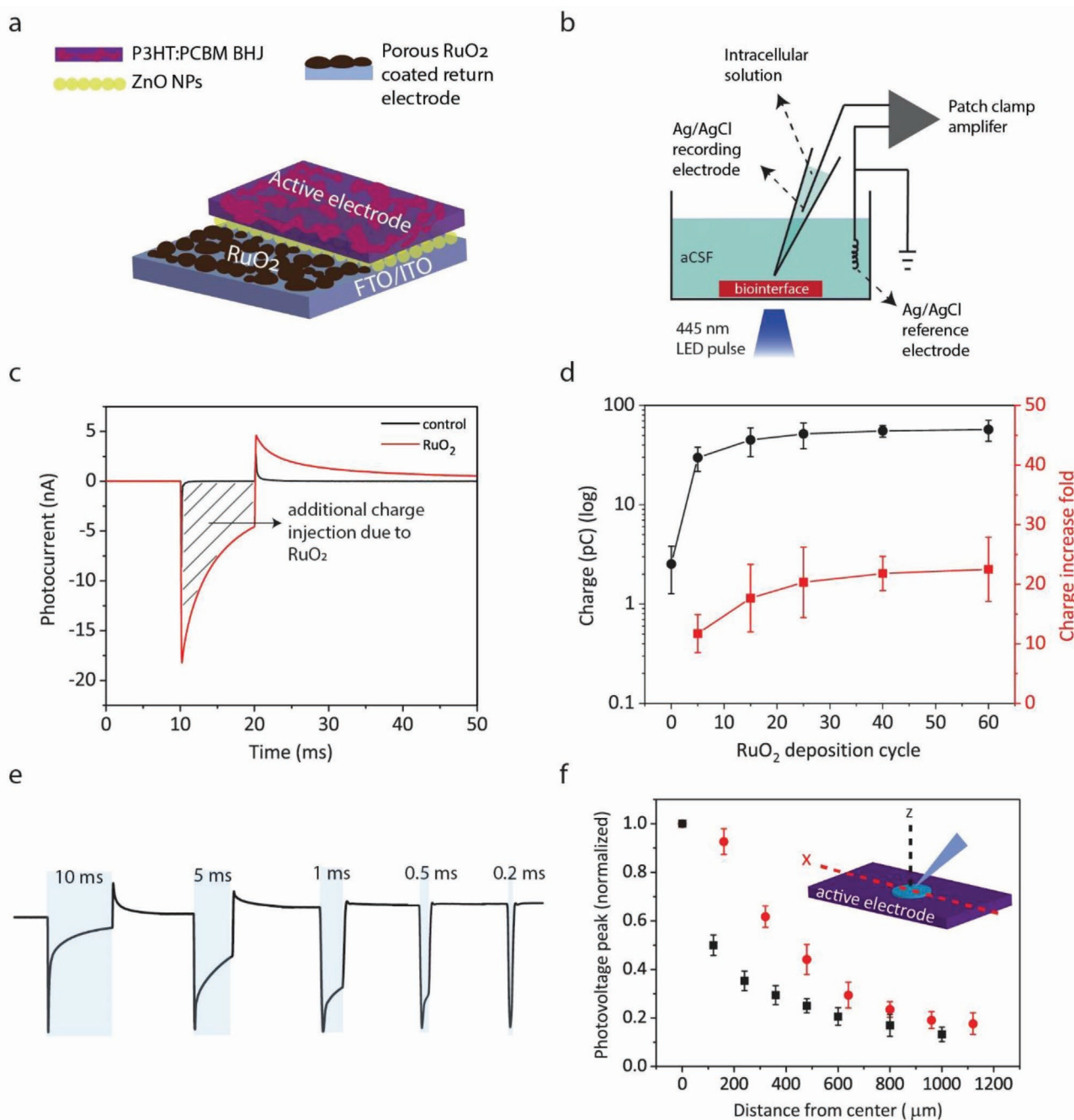


Figure 2. Effect of RuO₂ on the biointerface photoresponse. a) Schematic of the RuO₂ integrated biointerface architecture. Control device is the same structure without RuO₂ coating. b) Schematic of the photoresponse characterization setup. Stimulation light source is an LED (445 nm nominal wavelength, 2 mW mm⁻² optical power density) and the recording tool is a patch-clamp amplifier with a micropipette that is positioned less than 5 μm from the biointerface surface. c) Photocurrent generated by control and RuO₂ biointerfaces at the device–electrolyte interface. 10 ms light pulse with 2 mW mm⁻² optical power density was applied when $t = 10$ ms. The simplified equivalent circuit of the interface is shown in Figure S5 (Supporting Information). d) Injected charge levels extracted from the photocurrent measurements of control and RuO₂ biointerfaces (mean \pm s.d. for $n = 8$). Zero deposition cycle represents the control device. Right axis shows the amount of enhancement in the injected charge for each RuO₂ coating. e) Photocurrent responses of 60-cycle RuO₂ biointerface for different pulse-width illuminations. Shaded areas represent “light-on” periods. f) Spatial distribution of photovoltage at increasing distances from the illumination spot center horizontally (x) and vertically (z). Inset illustrates the measurement configuration, where the blue circle designates the illumination spot (320 μm diameter, 10 ms pulse).

of additional charge injection into the electrolyte due to the enhancement of the return electrode capacitance (Figure 2c).^[22] The steady photovoltage during illumination evokes reversible

Faradaic reactions on the RuO₂ surface, predominantly redox reactions of Ru⁴⁺/Ru³⁺ couple,^[14a,18] leading to formation of a redox capacitance, which is embedded in the redox impedance

of return electrode, in addition to the double-layer capacitance (Figure S5, Supporting Information). Considering that the double-layer capacitance of typical organic electrode–electrolyte interfaces is on the order of 1 to a few tens of $\mu\text{F cm}^{-2}$,^[5,23] the double-layer capacitance of RuO_2 –electrolyte interface is expected to be on the similar order. However, the redox impedance, which includes the pseudocapacitance of RuO_2 and is in parallel to the double-layer capacitance, significantly boosts the interfacial capacitance of the return electrode, which is counterbalanced by faradaic reactions at P3HT:PCBM–electrolyte interface (Figure S6, Supporting Information). As a result, the onset photocurrent peak increased more than two-fold (Figure S7, Supporting Information). Noticeably, the amount of the total charge injection substantially increased, which can be controlled with the deposition cycles. While the charge injection capacity of control devices was $2.5 \pm 1.3 \text{ pC}$ (mean \pm SD), for 5-cycle- RuO_2 biointerfaces it jumped to $29.8 \pm 8.1 \text{ pC}$ (mean \pm SD), indicating more than an order of magnitude increase. For 60 cycles, the injected charge reached $57.1 \pm 13.7 \text{ pC}$ (mean \pm SD), corresponding to over 20-fold enhancement compared to control devices (Figure 2d). If the counter-balancing faradaic reactions at P3HT:PCBM–electrolyte interface are suppressed, the charge injection performance of RuO_2 -based biointerfaces notably decreases (Figure S6, Supporting Information), which confirms that the observed improvement in photoresponse is due to the redox impedance of RuO_2 . As a further control experiment, we checked whether RuO_2 generates photocurrent by itself, and verified that RuO_2 layer alone produces only a marginal photocurrent, which is at least two orders of magnitude lower than the photovoltaic part (Figure S8, Supporting Information). Since the best performing device is 60 cycle RuO_2 , the rest of the experiments were conducted with 60 cycle RuO_2 biointerfaces (referred as “ RuO_2 BI” in the rest of the text).

Temporal characteristics of the generated photocurrent provide information about the maximum achievable stimulus frequencies. Figure 2e shows photocurrents of RuO_2 BI under pulsed illumination for pulse-widths of 10 ms, 5 ms, 1 ms, 500 μs , and 200 μs . The capacitive onset peak was preserved even for 200 μs pulse, implying that high-frequency stimulus, e.g., 100 Hz, can be applied via RuO_2 BI. For example, when we applied 1 ms 100 Hz pulsed excitation, the photocurrent peak and shape were well-preserved throughout the repeated photoexcitation cycles (Figure S9, Supporting Information). Lastly, we evaluated the spatial distribution of the photoresponse by measuring the photovoltage while moving the patch pipette in horizontal and vertical directions, starting from the center of the illumination spot (radius $R = 160 \mu\text{m}$; Figure 2f inset). Charge injection decays in an exponential fashion in both directions as the pipette was gradually moved away from the spot center (Figure 2f), suggesting a localized charge injection primarily governed by illumination spot area. In horizontal direction, the measured charge was still over 90% at the spot edge (1R away from the center) and it drops to 62% 2R away from the center. This represents a relatively slower decay compared to a previous study,^[6b] most likely due to the device geometry with large return electrode.

To quantify the short-circuit photoelectrical response of RuO_2 BI, we measured its photoresponse via a three-electrode

potentiostat/galvanostat system (Figure 3a). Working electrode was connected to the ITO back electrode, while the counter and reference electrodes were floating in the ionic aCSF medium.^[24] The intensity-dependent photocurrent and photovoltage measurements in Figure 3b,c showed the maximum achievable current density of 6 mA cm^{-2} and 290 mV photovoltage for RuO_2 BI under 445 nm 85 mW cm^{-2} LED illumination, respectively. Integrating the area under the photocurrent–time traces corresponds to the injected charges for each illumination intensity (Figure 3d) and RuO_2 BI has a charge injection density of more than $10 \mu\text{C cm}^{-2}$ for intensities greater than 30 mW cm^{-2} . This charge injection level is sufficiently high according to the reported threshold charge density values for stimulation of human epiretinal, cortical, auditory brainstem, and subthalamic nucleus neurons.^[19] In addition, RuO_2 BI has more than an order of magnitude higher charge injection capacity compared to control devices (Figure 3d).

Previously we showed that high-frequency stimulus (e.g., 100 Hz) via short pulses (e.g., 1 ms) can be applied with RuO_2 BI. Now, we demonstrate that even for such short pulse durations, the charge density of RuO_2 BI is in the $\mu\text{C cm}^{-2}$ range. For 1 ms pulse, injected charge density is $2.4 \pm 0.6 \mu\text{C cm}^{-2}$ (mean \pm SD), while it is $1.6 \pm 0.7 \mu\text{C cm}^{-2}$ (mean \pm SD) for 500 μs pulse (Figure 3e inset), which are still near the thresholds for stimulation of certain neural tissues (e.g., subthalamic nucleus, auditory brainstem).^[19] Moreover, for lower stimulus frequencies 20 ms pulse would result in a high charge density of $20.2 \pm 2.4 \mu\text{C cm}^{-2}$ (mean \pm SD; Figure 3e).

We tested the stability and biocompatibility of RuO_2 BI and checked whether repeated photoexcitation of RuO_2 BI causes reactive oxygen species (ROS) intake by neurons or not. Stability was studied by investigating the charge injection performance of RuO_2 BI after detailed tests including low-temperature sterilization, accelerated passive and reactive aging, and repeated photoexcitation experiments. Low-temperature hydrogen peroxide (H_2O_2) plasma sterilization is an FDA approved technique for testing medical devices.^[25] After application of low-temperature H_2O_2 plasma sterilization, the charge injection levels of RuO_2 BI reduced to $78\% \pm 9\%$ (mean \pm SD) of its pre-sterilization value (Figure 4a). The sterilized RuO_2 BI samples were further subjected to accelerated reactive aging test, where we kept the samples in H_2O_2 -added aCSF at 87 °C oven and quantified their charge injection performance after every 48 h, which corresponds to a simulated aging period of 2 months. After an aging period of 12 months, RuO_2 BI preserved $76\% \pm 8\%$ of its post-sterilization and $60\% \pm 6\%$ of its pre-sterilization charge injection values indicating robust operation of RuO_2 BI under harsh aging conditions (Figure 4b). At this point, we wondered whether the reduction in charge injection values of RuO_2 BI is due to the degradation of ZnO/P3HT:PCBM active electrode or RuO_2 coating. The EIS measurements of active electrode and RuO_2 coating before and after plasma sterilization and reactive aging tests showed that the impedance-frequency behavior of RuO_2 is preserved after the tests, while the response of active electrode deviated from its pre-sterilization behavior (Figure S10, Supporting Information). This implies that performance drop is primarily due to the degradation of the photoactive electrode, which can be prevented via gold layer deposition on top of the electrode;^[23c] and RuO_2

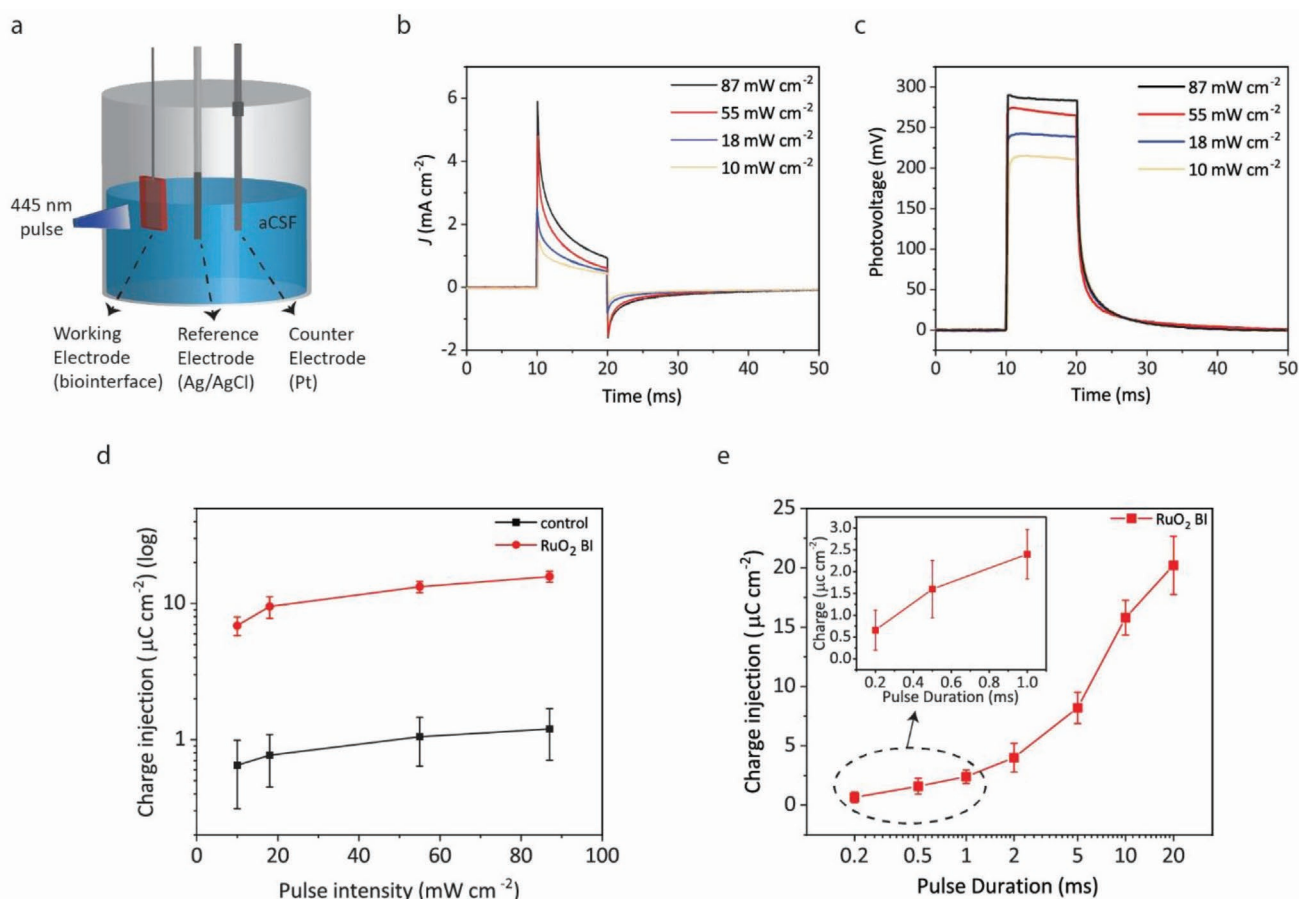


Figure 3. Photoelectrochemical performance of the optimized RuO₂ biointerface (RuO₂ BI). a) Illustration of the photocurrent/photovoltage measurement setup. Stimulation source is an LED (445 nm nominal wavelength, 10 ms pulses with optical power density ranging from 10 to 87 mW cm⁻²) and the recording tool is a three-electrode electrochemical setup connected to a potentiostat/galvanostat. 0.5 cm² of biointerface area is immersed in the aCSF electrolyte. b) Photocurrent density, and c) photovoltage of RuO₂ BI as a function of illumination intensity. Light pulse is applied when $t = 10$ ms. d) Injected charge into the aCSF electrolyte as a function of pulse intensity for control device and RuO₂ BI for 10 ms pulsed excitation (mean \pm SD for $n = 8$). e) Injected charge levels of RuO₂ BI for different pulse-width excitations (mean \pm SD for $n = 8$). Inset zooms into the first three data points encircled by the dashed ellipse.

remains intact under harsh aging conditions. Furthermore, RuO₂ BI exhibits excellent stability under passive accelerated aging test, showing no significant decrease in the charge injection performance after 24 months (Figure 4b). Moreover, the charge retention performance of RuO₂ BI was tested under repeated 10 000 cycle pulsed photoexcitation. After 10 000 illumination cycle, 84% \pm 5% of injected charge and the capacitive current profile (Figure 4c inset) are preserved, implicating the retained functionality of the biointerfaces (Figure 4c).

To evaluate the cytotoxicity of RuO₂ BI, we conducted in vitro biocompatibility test with primary hippocampal neurons via MTT toxicity assay and immunofluorescence imaging before and after 14 days of neuron culture. MTT analysis showed that neurons on RuO₂ BI demonstrate a statistically nonsignificant difference of cell viability compared to biocompatible ITO samples after 48 h incubation period (Figure 4d). This result is supported by immunofluorescence images of ITO and RuO₂ BI samples. Day 0 and day 14 images of ITO and RuO₂ BI demonstrated preserved cell viability and morphology for both sample types, suggesting low cytotoxicity of RuO₂ BI for in-vitro primary hippocampal neurons (Figure 4e).

Despite the reversibility of RuO₂-induced redox reactions, we wanted to reassure that RuO₂ BI does not generate ROS in the electrolyte upon photoexcitation. To validate that, we quantified the amount of ROS intake of hippocampal neurons cultured on RuO₂ BI by measuring the fluorescence intensity of H₂-DFCDA agent after subjecting the biointerfaces to 10 000-cycle photoexcitation (Figure 4g). We used neurons on bare FTO as negative control, on bare FTO treated with 100 μ M H₂O₂ as positive control, and on RuO₂ BI before photostimulation as control groups. Expectedly, neurons on positive control samples show high fluorescence intensity due to the intake of H₂O₂ in the extracellular medium. On the other hand, there is no statistical difference between the fluorescence intensities of neurons grown on bare FTO, RuO₂ BI before photostimulation, and RuO₂ BI after photostimulation (Figure 4f). Hence, repeated photoexcitation of RuO₂ BI does not cause intracellular oxidative stress for neurons, which indicates the absence of ROS formation in the aCSF. This suggests a safe photostimulation mechanism for RuO₂ BI. This is further supported by the pH measurement of extracellular medium during 40000-cycle photoexcitation of

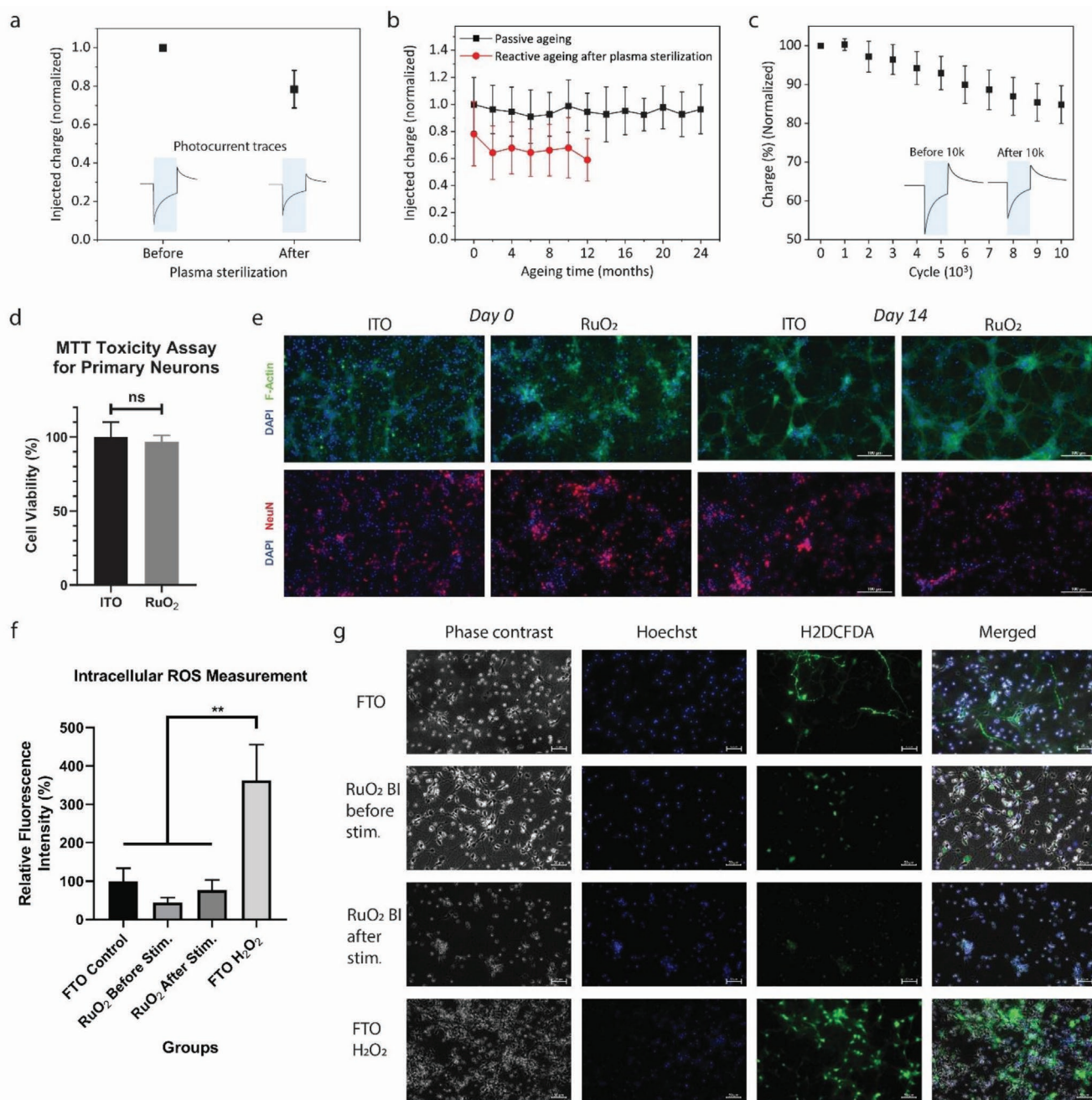


Figure 4. Stability, biocompatibility, and intracellular oxidative stress analysis. a) Charge injection performance of RuO₂ BI before and after low temperature H₂O₂ plasma sterilization (mean \pm SD for $n = 3$). The sum of three RuO₂ BI before the sterilization is normalized to 1. Inset shows photocurrent traces before and after the sterilization. b) Variation of RuO₂ BI charge injection levels during the passive and reactive accelerated ageing tests (mean \pm SD for $n = 3$). Reactive ageing test was applied to the biointerfaces that underwent plasma sterilization. c) Photocyclic stability of RuO₂ BI showing the variation of injected charge during the application of 10 000 photoexcitation pulse (mean \pm SD for $n = 4$). Illumination: 5 Hz stimulus frequency, 10 ms pulse-width, 2 mW mm⁻² optical power density. Inset shows photocurrent traces before and after 10 000 photocycles. d) MTT assay analysis for quantifying cell viabilities of primary hippocampal neurons cultured on RuO₂ BI (mean \pm SD for $n = 4$). Bare ITO sample, which is known to be biocompatible, was used as control. The level of significance was calculated using an unpaired, two-tailed *t*-test; * $p < 0.05$ was evaluated as statistically significant. e) Immunofluorescence images of ITO and RuO₂ BI samples obtained on day 0 and day 14 to observe the cell viability and morphology of hippocampal neurons after 14 days of culture. f) Quantification of ROS intake, i.e., intracellular oxidative stress, of neurons cultured on RuO₂ BI after subjecting the biointerfaces to 10 000 photoexcitation cycle (mean \pm SD for $n = 3$). Illumination: 5 Hz stimulus frequency, 10 ms pulse-width, 2 mW mm⁻² optical power density. RuO₂ before stimulation samples are control, bare FTO is negative control, bare FTO with H₂O₂ is positive control. The fluorescence intensity of negative control is normalized to 100%. g) Fluorescence microscope images of FTO, RuO₂ BI before stimulation, RuO₂ BI after stimulation and FTO with H₂O₂ samples stained with Hoechst and H2DCFDA, which were used to calculate the relative intracellular fluorescence intensities.

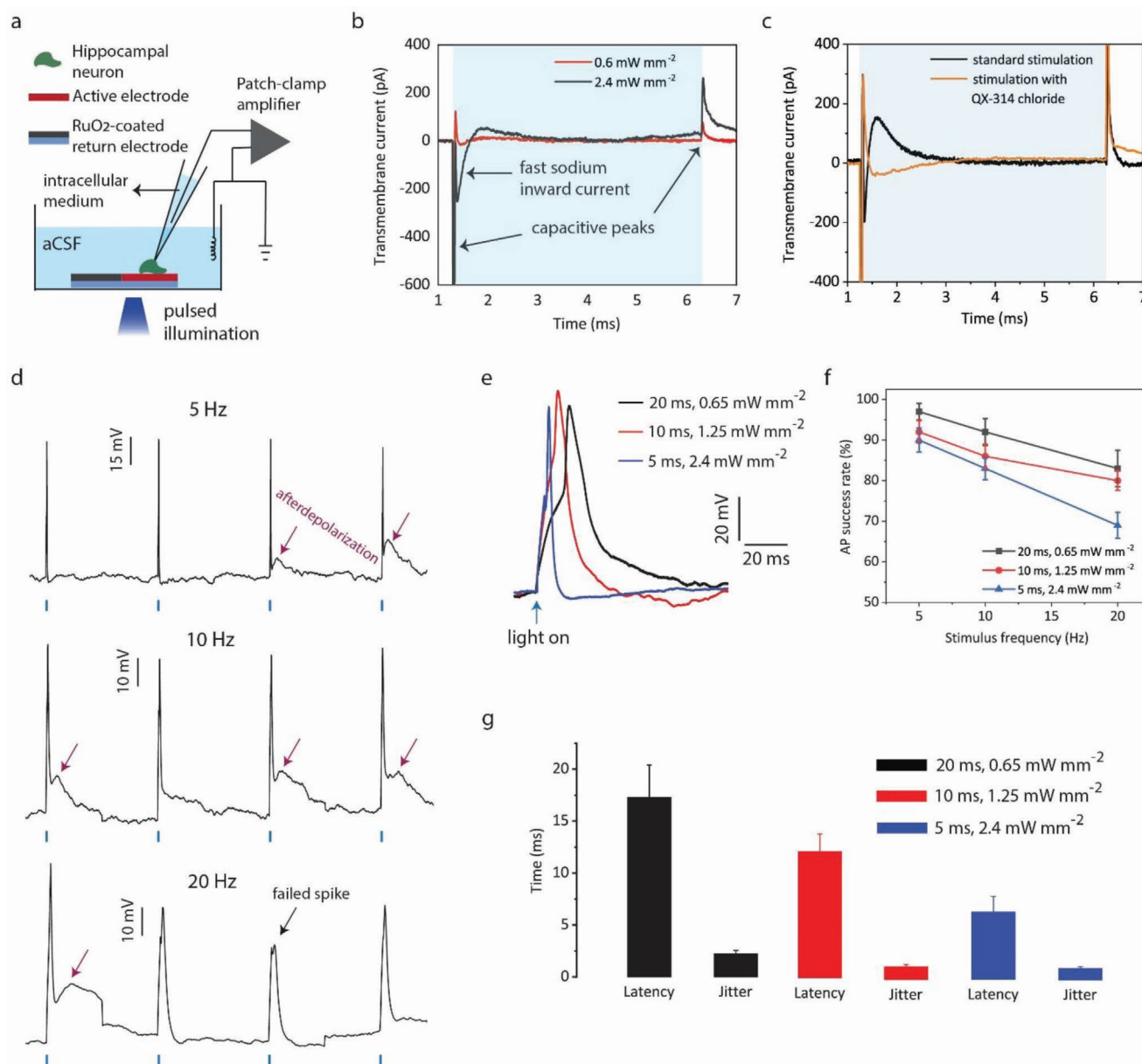


Figure 5. Photostimulation of primary hippocampal neurons via RuO₂ BI. **a**) Schematic of single-cell patch-clamp electrophysiology setup under illumination for light-triggered intracellular membrane voltage and current characterization with respect to a distant Ag/AgCl electrode. **b**) Membrane current in whole-cell voltage-clamp mode under different light-intensity illuminations (λ = 445 nm). Shaded area indicates the applied light duration period of 5 ms. **c**) Membrane current of neurons under standard conditions and after blocking the voltage-gated sodium channels via QX-314 chloride. Illumination parameters: 445 nm, 5 ms pulse-width, 2.4 mW mm⁻² light intensity. Shaded area indicates the 5 ms light-pulse period. **d**) Reproducible firing of hippocampal neurons for 5, 10, and 20 Hz stimulus frequencies. Illumination parameters: λ = 445 nm, 5 ms pulse-width, 2.4 mW mm⁻² light intensity. Blue bars indicate the start of pulses. Purple arrows show afterdepolarization occurrences. For action potential traces, the capacitive artefacts at the onset and offset of light were eliminated because of downsampling the current-clamp data (Figure S13, Supporting Information). Action potentials for 10 and 20 ms pulses were shown in Figure S14 (Supporting Information). **e**) Action potential traces for 5, 10, 20 ms pulse-widths with minimum power densities required to elicit firing. Each trace is the average of ten different spikes. **f**) Action potential success rates of 5, 10, 20 ms pulses for 5, 10, 20 Hz stimulus frequencies (mean ± SD for n = 10). **g**) Mean latency and jitter for 5, 10, 20 ms pulsed stimulations. Latency is the time between light-onset and action potential peak, while jitter is the standard deviation of latencies (mean ± SD for n = 10).

RuO₂ BI (Figure S11, Supporting Information). pH values measured after each 10 000-cycle photoexcitation do not show significant differences, implying that the chemical composition of aCSF is not altered by irreversible faradaic processes during repeated photoexcitation.

We finally explored the light-induced effect of RuO₂ BI on primary hippocampal neurons by measuring single-cell intracellular membrane potential and current with respect to a distant Ag/AgCl electrode via a patch-clamp setup. **Figure 5a** illustrates the measurement configuration, where RuO₂ BI is

operating wirelessly (i.e., electrically floating in aCSF) to photo-stimulate the cultured neurons. First, we checked if photoexcitation of RuO₂ BI can open voltage-gated sodium channels and induce inward sodium current, which is an essential component for eliciting action potential. As an initial control experiment, we measured the current–voltage characteristics of hippocampal neurons under dark conditions by applying different membrane holding voltages via the amplifier (Figure S12, Supporting Information). Rapid negative inward currents, which originate from voltage-gated sodium channels, start to appear at holding voltage of −50 mV. These sodium inward currents for −50, −30, and −10 mV holding potentials are followed by slower outward potassium currents (Figure S12a, Supporting Information). When we add voltage-gated sodium channel blocker QX-314 chloride^[26] into the intracellular solution, negative inward currents are no longer observed, confirming that they are due to voltage-gated sodium channels (Figure S12b, Supporting Information). Under light conditions without any external stimulus from amplifier, photoexcitation of RuO₂ BI with 5 ms pulses of 2.4 mW mm^{−2} illumination intensity induced fast sodium inward currents followed by a slower outward potassium current, a typical current profile observed during an action potential (Figure 5b).^[27] Lower light intensity, 0.6 mW mm^{−2}, did not result in the same response, which possibly led to a sub-threshold stimulation. As a control experiment, we added QX-314 chloride to the intracellular solution. As in the previous experiment, since photoexcitation of RuO₂ BI leads to rapid sodium inward current and slower outward potassium current for neurons under standard conditions, the inward sodium current is nearly vanished in the existence of QX-314 chloride (Figure 5c). These experiments denote that RuO₂ BI activates voltage-gated sodium channels of hippocampal neurons upon photoexcitation, which is expected to elicit action potentials.

To verify the firing of neurons, we conducted current-clamp recordings to examine their intracellular membrane potential with respect to a distant Ag/AgCl electrode. The recordings demonstrate that light-induced photoresponse of RuO₂ BI reproducibly stimulates neurons under 5 ms pulsed excitation with stimulus frequencies of 5, 10, and 20 Hz (Figure 5d). Evoked action potentials are temporally precise and some peaks are followed by afterdepolarizations, which frequently occur during firing of hippocampal neurons.^[28] The spikes with 5 ms pulses are induced by minimum 2.4 mW mm^{−2} light intensity. Figure 5e displays that longer pulses with lower illumination intensities, 10 ms at 1.25 mW mm^{−2} and 20 ms at 0.65 mW mm^{−2}, can also elicit action potentials. As pulse-width increases, the minimum required power for photoactivation decreases. However, the minimum total energy for evoking action potentials stays nearly constant as expected for extracellular stimulation electrodes.^[29] The resultant action potential success rates show similar fashions for 5, 10, and 20 ms pulses, showing slight decrease as the stimulus frequency is increased. The success rates stay above 80% for all pulse-widths and stimulus frequencies, except for 5 ms 20 Hz pulse, for which it is 69% ± 3 (mean ± s.d.) (Figure 5f). Higher success rates for longer pulse-widths are ascribed to continuous charge injection during light-on periods due to RuO₂ return electrode. On the other hand, action potential latencies are directly proportional with the pulse-widths (Figure 5g). Overall, the electrophysiology

recordings signify the effective photostimulation performance of RuO₂ BI indicated by temporal precision, rapid reversibility, and short latencies.

3. Discussion

This study demonstrated the potential of pseudocapacitive material of RuO₂ to realize highly light-sensitive organic optoelectronic biointerfaces. One major obstacle for organic optoelectronic biointerfaces, especially capacitive ones, has been the difficulty of achieving high photogenerated charge densities,^[5] and the proposed strategy in this report can be an important step toward realizing much-elevated charge injection densities. Although other alternatives such as dielectric SiO₂ coating and pseudocapacitive PEDOT:PSS coating were used to enhance the interfacial capacitance,^[10,30] our findings show that RuO₂ distinctively outperforms those materials in terms of their contribution to charge injection densities. Moreover, the increased charge injection efficiency allows for neurostimulation with shorter pulses and latencies that can enable improved temporal control.

Advantageously, RuO₂ can be directly integrated into a wide variety of device architectures^[5,6] to improve the device performance levels via the low-cost electrodeposition technique and even on non-planar substrates. Comparatively, iridium oxide in the form of SIROF was shown to perform well in a silicon-based planar photodiode architecture in terms of its contribution to charge injection performance,^[31] however, sputtering is a relatively complex and expensive method compared to solution-processing techniques. Recently it was demonstrated that sputtered RuO₂ exhibits similar charge storage/charge injection performances with SIROF, indicating its high potential for electrical stimulation/recording electrodes.^[14] Here, electrodeposition of RuO₂ also performs at similar levels of SIROF and sputtered RuO₂, together with the advantage of simple device fabrication. Stability, biocompatibility, and safe stimulation pathway through highly reversible charge transfer reactions demonstrated by intracellular oxidative stress measurements of RuO₂-based biointerface show promise for in vivo applications. Moreover, the effective performance of RuO₂ can motivate the investigation of alternative pseudocapacitive coating materials for neural interfaces. Carbon materials (e.g., carbide-derived carbon), metal oxides (e.g., manganese oxide), and conducting polymers (e.g., polypyrrole) can be effective due to their high capacitance, low toxicity, and reversible charge injection mechanisms.^[11a]

In conclusion, our findings pave the way toward building safe and highly efficient optoelectronic biointerfaces by using pseudocapacitive RuO₂. The biointerfaces showed improved photoelectrical performance parameters compared to control samples, i.e., increased capacitive photocurrent peak and higher charge storage/injection efficiencies. Detailed electrochemical analysis of RuO₂ coating revealed the reversible nature of redox reactions, indicating a safe charge injection mechanism for RuO₂-based optoelectronic biointerfaces, which was further supported by intracellular ROS measurements. Excitation of RuO₂-based biointerfaces via short light pulses can activate voltage-gated sodium channels, which leads to reproducible action potential firing on primary hippocampal neurons.

Consequently, the safe and efficient stimulation mechanism obtained by simple solution-processed RuO₂ integration shows great promise for building flexible, low-cost, biocompatible, stable, and highly light-sensitive optoelectronic biointerfaces for future retinal prosthesis.

4. Experimental Section

Biointerface Fabrication: ITO/PET (Sigma Aldrich, 639303) and FTO/glass substrates (Ossila, TEC 10) were cleaned by sonication in detergent solution, deionized water, acetone, and isopropanol consecutively for 15 min each, followed by 20 min UV ozone treatment. Poly(3-hexylthiophene-2,5-diyl) (P3HT) with regioregularity of 95.7% and a molecular weight of 57467 g mol⁻¹ (Ossila) and [6,6]-PPhenyl-C61-butyric acid methyl ester (PC61BM) with a molecular weight of 1031 g mol⁻¹ were supplied by Ossila Ltd. 1,2-dichlorobenzene solutions of P3HT (20 mg mL⁻¹) and PCBM (12 mg mL⁻¹) were prepared and stirred at 70 °C overnight. P3HT and PCBM solutions were mixed (1:1 volume ratio) and stirred for further 2 h using magnetic stirrer. ZnO precursor sol-gel solution (0.45 M) was prepared by mixing 219.3 mg Zinc acetate dehydrate (Zn(CH₃COO)₂·2H₂O), 2 mL of 2-Methoxyethanol (C₃H₈O₂) and 73 mg of Ethanolamine (HOCH₂CH₂NH₂). Ruthenium (III) chloride hydrate (RuCl₃·H₂O) with molecular weight of 207.43 g mol⁻¹ was purchased from Sigma-Aldrich. Aqueous solution (0.01 M) of RuCl₃·H₂O was prepared for electrochemical deposition of ruthenium oxide (RuO₂).

For the fabrication of RuO₂-based biointerfaces, first, a certain area of FTO/ITO substrate, where RuO₂ will be coated, was covered with a mask. Then, ZnO precursor sol-gel solution was spin-coated on the remaining area of the substrate at 2000 rpm, followed by 15 min annealing at 290 °C for FTO and 20 min at 200 °C for ITO. On ZnO layer, P3HT:PCBM solution was spin-coated at 2000 rpm, followed by 15 min annealing at 150 °C. Then, the mask was removed. The area under the mask was immersed into 0.01 M aqueous solution of RuCl₃·H₂O and RuO₂ layer was formed via cyclic voltammetric deposition by cycling the potential between -0.2 and 1.2 V at a scan rate of 50 mV s⁻¹.

Photoresponse Analysis: Interfacial (open-circuit) photocurrents were recorded via EPC 800 Heka Elektronik patch-clamp amplifier in voltage-clamp mode using patch pipettes (6–8 MΩ). Biointerfaces were placed in aCSF, which consists of 10 × 10⁻³ M of 4-(2-hydroxyethyl)-1-piperazineethanesulfonic acid (HEPES), 10 × 10⁻³ M of glucose, 2 × 10⁻³ M CaCl₂, 140 × 10⁻³ M of NaCl, 1 × 10⁻³ M of MgCl₂, and 3 × 10⁻³ M of KCl. The pH of aCSF solution was adjusted to 7.4 by adding a stoichiometric amount of NaOH. Patch pipettes were filled with intracellular medium, which consisted of 140 × 10⁻³ M KCl, 2 × 10⁻³ M MgCl₂, 10 × 10⁻³ M HEPES, 10 × 10⁻³ M ethylene glycol-bis(β-aminoethyl ether)-N,N,N',N'-tetraacetic acid (EGTA), and 2 × 10⁻³ M Mg-ATP dissolved in distilled water. The pH of the intracellular solution was adjusted to 7.2–7.3 by adding a stoichiometric amount of KOH.

Chronopotentiometry and chronoamperometry measurements were performed via Autolab Potentiostat Galvanostat PGSTAT302N (Metrohm, Netherlands) using a three-electrode setup consisting of Ag/AgCl as the reference electrode, platinum rod as the counter electrode, and the thin film samples as the working electrode in aCSF solution.

Light pulses were applied via Thorlabs M450LP1 LED with 445 nm nominal wavelength and the LED spectrum was provided in the previous study.^[23c] The blue LED was driven with Thorlabs DC2200 – High-Power 1-Channel LED Driver. Newport 843-R power meter was used to measure the optical power of incident light on the biointerfaces.

Electrochemical Measurements: Autolab Potentiostat Galvanostat PGSTAT302N (Metrohm, Netherlands) was used for cyclic voltammetry (CV) and electrochemical impedance spectroscopy (EIS) measurements. Three-electrode electrochemical setup consisted of Ag/AgCl reference electrode, platinum rod counter electrode, and the thin-film biointerface samples as working electrode. The EIS was performed in frequency response analysis (FRA) potential scan mode while varying the frequency between 1 Hz and 10 kHz at 10 mV (RMS)

AC voltage perturbation. The fitting of the high-frequency resistance and low-frequency capacitance was performed in NOVA software to extract the corresponding circuit parameters. A more detailed fit can be performed via a 3-RC circuit, however the extra detail would be a distraction and not add to the main argument of the paper. Therefore, only the high-frequency resistance and the low-frequency capacitance are considered.

Primary Neuron Isolation: All experimental procedures have been approved by the Institutional Animal Care and Use Committees of Koç University (Approval No: 2019.HADYEK.023) according to Directive 2010/63/EU of the European Parliament and of the Council on the Protection of Animals Used for Scientific Purposes. Hippocampal regions were extracted from decapitated E15-E17 Wistar Albino rat embryos and were placed immediately in ice-cold Hank's Balanced Salt Solution (HBSS, Thermo Fisher Scientific, MA, USA). The hippocampi were incubated in 0.25% Trypsin-EDTA solution (Thermo Fisher Scientific, MA, USA) with 2% DNase-I supplement (NeoFroxx, Einhausen, Germany) for 20 min in a 37 °C incubator. Then the cells were centrifuged, and the supernatant was changed with Dulbecco's Modified Eagle Medium/Nutrient Mixture F-12 (DMEM/F12 Thermo Fisher Scientific, MA, USA) supplemented with 10% fetal bovine serum (FBS, Heat Inactivated, GE Healthcare, IL, USA) and 1% penicillin/streptomycin (Thermo Fisher Scientific, MA, USA). DMEM/F12 was removed and Neurobasal Medium (NBM, Thermo Fisher Scientific, MA, USA) supplemented with B27, L-glutamine, β-mercaptoethanol, glutamate (Thermo Fisher Scientific, MA, USA) was added to the cell pellet. The cells were triturated and were passed through a 70 μm cell strainer. The homogenous cell solution was seeded in poly-D-lysine (PDL, Sigma-Aldrich, MO, USA) coated substrates. After 3-days incubation of cells on substrates in a 37 °C incubator with 5% carbon dioxide, the media of the cells on substrates were changed with NBM supplemented with cytosine arabinoside (Sigma-Aldrich, MO, USA) to inhibit the growth of glial cells. After 24-h incubation with cytosine arabinoside, the media were changed with NBM and the substrates with the hippocampal neurons used for the experiments.

Biocompatibility Assay: MTT viability assay was applied to investigate the cell viability of primary hippocampal neurons on the biointerfaces. The neural growth medium was prepared by using B27 supplemented Neurobasal medium. MTT cell viability assay (Abcam, ab211091) was utilized to evaluate biocompatibility of our biointerface. The devices were sterilized first by cleaning with 70% ethanol followed by air-drying. The surface was further sterilized under UV irradiation for 30 min. Substrates were placed in wells of the six-well plates. Primary hippocampal neurons were seeded (5 × 10⁵ cells per sample) on the substrates in B27-supplemented Neurobasal medium as described above and incubated in the neuron growth medium for 48 h after cytosine arabinoside supplemented neurobasal medium removal. After 48 h incubations, the media were replaced with 1 mL of MTT solution (5 mg mL⁻¹ in PBS, pH 7.4) and 4 mL of NBM mixture per well. Then, for an additional 4 h, the cells were incubated at 37 °C and 5% CO₂ atmosphere. The medium was vacuumed from each well and substrates were transferred to empty six-well plates. In each well, 1:1 mixture of DMSO and ethanol was added to dissolve the formazan crystals. The solution was transferred to a 96-well plate and the absorbance was measured at 570 nm light with Synergy H1 Microplate Reader (Bio-Tek Instruments). The relative cell viability was calculated as follows: Viability = (OD_{sample}/OD_{control}) × 100. The optical density (OD) of the sample was obtained from the cells grown on a photoelectrode, and the OD of control was obtained from the cells grown on the ITO substrates.

Immunofluorescence Staining and Imaging: Primary hippocampal neurons (5 × 10⁵ cells per sample) were seeded as explained above on ITO control substrate and the biointerface. The samples with neurons were fixed by 4% paraformaldehyde immediately after primary hippocampal neuron isolation protocol or incubated for 14 days with regular medium changes at 37 °C in the cell culture incubator. After 14-day incubation, the primary hippocampal neurons were also fixed by 4% paraformaldehyde and washed three times with PBS-T (Phosphate Buffered Saline, 0.1% Triton X-100). Cells were blocked in PBS solution

containing 5% BSA (Bovine Serum Albumin) and 0.1% Triton X-100. Samples with primary hippocampal neurons were incubated with rabbit anti-NeuN antibody (ab177487, Abcam, Cambridge, UK) overnight, for neuron characterization, and washed three times with PBS-T. Then, samples with primary hippocampal neurons were incubated with goat anti-rabbit IgG H&L Alexa Fluor 555(4413, Cell Signaling Technology, MA, USA) for fluorophore marking of anti-NeuN primary antibody for 90 min at 37 °C. For visualization of the cytoskeleton, primary neuron samples also were incubated with FITC-conjugated phalloidin antibody (Sigma-Aldrich, P5282) for 90 min at 37 °C. All samples were washed three times with PBS-T, then mounted with DAPI supplemented mounting medium (ab104139, Abcam, Cambridge, UK) to observe nuclei. Finally, immunofluorescence imaging was done using a fluorescence light microscope (Axio Observer Z1, ZEISS, Oberkochen, Germany).

Intracellular Oxidative Stress Measurement: The intracellular oxidative stress level was measured by 2',7'-dichlorodihydrofluorescein diacetate (H₂DFCDA) (D399, Molecular Probes, Invitrogen). Primary hippocampal neurons (5 × 10⁵ cells per sample) were seeded on FTO control substrates and the biointerfaces. The H₂DFCDA agent is nonfluorescent but it becomes intensive fluorescent agent after oxidation with H₂O₂. Thus, as a positive control group, neurons grown on the control substrates were treated with 100 × 10⁻⁶ M H₂O₂ for 30 min. In the experimental group, neurons grown on the biointerfaces were exposed to 450 nm LED for 10 000 cycles with 5 Hz frequency. Cells were washed once with PBS and then incubated with 20 × 10⁻⁶ M H₂DFCDA in aCSF solution for 45 min prior to imaging at 37 °C, 5% CO₂ to allow H₂DFCDA to fully enter the cells. Hoechst (0.6 mg mL⁻¹) was used to stain the nucleus for 15 min at 37 °C, 5% CO₂. To avoid remaining dye residues, cells were washed with PBS. To avoid photobleaching, all steps were carried out in the dark. All immunofluorescence images were taken in the same light intensity, exposure, time point, and magnification with live-cell fluorescence microscope (Axio Observer Z1, ZEISS, Oberkochen, Germany) and average fluorescence intensity was measured by ImageJ software (ImageJ Fiji, NIH, MD, USA). For image analysis, images were converted to 8-bit black and white image and background was subtracted. To measure number and area of cells, maximum entropy threshold was applied to the image and the particles were analyzed for integrated density. By this way, both area of neurons and intensity of fluorescence were measured in acquired images from randomly selected ten different regions of neural cell culture. Relative fluorescence intensity was calculated with negative (neurons on FTO substrate) and positive (neurons on FTO with H₂O₂ addition to induce ROS production) controls. Normal ROS production in FTO control substrates was accepted as 100% in relative fluorescence intensity comparison.

Electrophysiology Recordings: Single-cell electrophysiology experiments were performed using EPC 800 Heka Elektronik patch-clamp amplifier in whole-cell configuration. Biointerfaces were electrically floating in aCSF without any wire connection. Whole-cell transmembrane voltage and current recordings, which refer to intracellular membrane potential and current recordings with respect to a distant Ag/AgCl electrode, were taken in current-clamp and voltage-clamp modes, respectively. Downsampling was applied to the current-clamp data to obtain a feasible computational complexity for making statistical analysis of action potentials without causing loss of any meaningful data. The patch pipette resistance of 6–8 MΩ was used for the recordings. The biointerfaces were placed in aCSF and patch pipettes were filled with the intracellular medium. To block the voltage-gated sodium channels, 5 × 10⁻³ M QX-314 chloride was added into the intracellular solution. Patch pipette and cells were monitored through a digital camera integrated with the Olympus T2 upright microscope.

Supporting Information

Supporting Information is available from the Wiley Online Library or from the author.

Acknowledgements

The authors gratefully acknowledge the use of the facilities and services of the Koc University Surface Science and Technology Center (KUYTAM). The authors gratefully acknowledge use of the services and facilities of the Koç University Research Center for Translational Medicine (KUTTAM), funded by the Republic of Turkey Ministry of Development. The content is solely the responsibility of the authors and does not necessarily represent the official views of the Ministry of Development. This project received funding from the European Research Council (ERC) under the European Union's Horizon 2020 Research and Innovation Programme (grant agreement no. 639846). S.N. acknowledges the Turkish Academy of Sciences (TÜBA-GEBİP) and Science Academy (BAGEP).

Conflict of Interest

The authors declare no conflict of interest.

Author Contributions

O.K. and S.N. designed the experiments. O.K. fabricated and characterized the biointerfaces, performed photoresponse measurements and electrophysiology experiments. E.Y. performed primary hippocampal neuron isolation, biocompatibility assay, immunofluorescence staining, and imaging of primary hippocampal neurons. H.N.K. conducted intracellular oxidative stress measurements. B.U. supervised the electrochemistry experiments and interpreted the data. A.S. supervised the cell culture, biocompatibility, immunofluorescence imaging, and intracellular oxidative stress experiments and interpreted the data. O.K. and S.N. wrote the manuscript with input from all authors. All authors contributed to the article and confirmed the submitted version.

Data Availability Statement

The data that support the findings of this study are available from the corresponding author upon reasonable request.

Keywords

biointerfaces, neural interfaces, organic bioelectronics, photostimulation, supercapacitors

Received: September 15, 2021

Revised: April 21, 2022

Published online: May 12, 2022

- [1] a) A. L. Benabid, *Curr. Opin. Neurobiol.* **2003**, *13*, 696; b) R. V. Shannon, *Curr. Opin. Neurol.* **2012**, *25*, 61; c) H. S. Mayberg, A. M. Lozano, V. Voon, H. E. McNeely, D. Seminowicz, C. Hamani, J. M. Schwab, S. H. Kennedy, *Neuron* **2005**, *45*, 651; d) R. Fisher, V. Salanova, T. Witt, R. Worth, T. Henry, R. Gross, K. Oommen, I. Osorio, J. Nazzaro, D. Labar, *Epilepsia* **2010**, *51*, 899.
- [2] S. H. Yun, S. J. Kwok, *Nat. Biomed. Eng.* **2017**, *1*, 0008.
- [3] Y. Jiang, X. Li, B. Liu, J. Yi, Y. Fang, F. Shi, X. Gao, E. Sudzilovsky, R. Parameswaran, K. Koehler, *Nat. Biomed. Eng.* **2018**, *2*, 508.
- [4] a) H. Lorach, G. Goetz, R. Smith, X. Lei, Y. Mandel, T. Kamins, K. Mathieson, P. Huie, J. Harris, A. Sher, *Nat. Med.* **2015**, *21*, 476; b) K. Mathieson, J. Loudin, G. Goetz, P. Huie, L. Wang, T. I. Kamins,

- L. Galambos, R. Smith, J. S. Harris, A. Sher, *Nat. Photonics* **2012**, 6, 391.
- [5] D. Rand, M. Jakešová, G. Lubin, I. Věbraité, M. David-Pur, V. Đerek, T. Cramer, N. S. Sariciftci, Y. Hanein, E. D. Głowacki, *Adv. Mater.* **2018**, 30, 1707292.
- [6] a) D. Ghezzi, M. R. Antognazza, M. Dal Maschio, E. Lanzarini, F. Benfenati, G. Lanzani, *Nat. Commun.* **2011**, 2, 166. b) D. Ghezzi, M. R. Antognazza, R. Maccarone, S. Bellani, E. Lanzarini, N. Martino, M. Mete, G. Pertile, S. Bisti, G. Lanzani, *Nat. Photonics* **2013**, 7, 400; c) M. Jakešová, M. S. Ejneby, V. Đerek, T. Schmidt, M. Gryszel, J. Brask, R. Schindl, D. T. Simon, M. Berggren, F. Elinder, *Sci. Adv.* **2019**, 5, eaav5265; d) J. F. Maya-Vetencourt, D. Ghezzi, M. R. Antognazza, E. Colombo, M. Mete, P. Feyen, A. Desii, A. Buschiazzi, M. Di Paolo, S. Di Marco, *Nat. Mater.* **2017**, 16, 681.
- [7] D. R. Merrill, M. Bikson, J. G. Jefferys, *J. Neurosci. Methods* **2005**, 141, 171.
- [8] A. González, E. Goikolea, J. A. Barrena, R. Mysyk, *Renewable Sustainable Energy Rev.* **2016**, 58, 1189.
- [9] K. Hou, C. Yang, J. Shi, B. Kuang, B. Tian, *Small* **2021**, 17, 2100165.
- [10] a) M. Silverà Ejneby, L. Migliaccio, M. Gicevičius, V. Đerek, M. Jakešová, F. Elinder, E. D. Głowacki, *Adv. Mater. Technol.* **2020**, 5, 1900860; b) M. Han, S. B. Srivastava, E. Yildiz, R. Melikov, S. Surme, I. B. Dogru-Yuksel, I. H. Kavakli, A. Sahin, S. Nizamoglu, *ACS Appl. Mater. Interfaces* **2020**, 12, 42997.
- [11] a) P. Simon, Y. Gogotsi, *Nanoscience and technology: a collection of reviews from Nature journals* **2010**, 320; b) J. R. Miller, P. Simon, *Sci. Mag.* **2008**, 321, 651.
- [12] N. Muhammad, Z. Guo, *Current Opin. Chem. Biol.* **2014**, 19, 144.
- [13] a) Z. Xiao, X. Jiang, B. Li, X. Liu, X. Huang, Y. Zhang, Q. Ren, J. Luo, Z. Qin, J. Hu, *Nanoscale* **2015**, 7, 11962; b) A. Ananth, S. Dharaneedharan, M. S. Gandhi, M.-S. Heo, Y. S. Mok, *Chemical Eng. J.* **2013**, 223, 729; c) Z. Liu, L. Xie, K. Qiu, X. Liao, T. W. Rees, Z. Zhao, L. Ji, H. Chao, *ACS Appl. Mater. Interfaces* **2020**, 12, 31205.
- [14] a) B. Chakraborty, A. Joshi-Imre, J. Maeng, S. F. Cogan, *J. Biomed. Mater. Res., Part B* **2021**, 109, 643; b) R. Atmaramani, B. Chakraborty, R. T. Rihani, J. Usoro, A. Hammack, J. Abbott, P. Nnoromele, B. J. Black, J. J. Pancrazio, S. F. Cogan, *Acta Biomater.* **2020**, 101, 565.
- [15] I. Ryu, M. Yang, H. Kwon, H. K. Park, Y. R. Do, S. B. Lee, S. Yim, *Langmuir* **2014**, 30, 1704.
- [16] C.-C. Hu, K.-H. Chang, M.-C. Lin, Y.-T. Wu, *Nano Lett.* **2006**, 6, 2690.
- [17] a) K. Kim, N. Winograd, *J. Catal.* **1974**, 35, 66; b) J.-J. Jow, H.-J. Lee, H.-R. Chen, M.-S. Wu, T.-Y. Wei, *Electrochim. Acta* **2007**, 52, 2625.
- [18] I.-H. Kim, K.-B. Kim, *J. Electrochem. Soc.* **2006**, 153, A383.
- [19] S. F. Cogan, *Annu. Rev. Biomed. Eng.* **2008**, 10, 275.
- [20] O. Karatum, G. O. Eren, R. Melikov, A. Onal, C. W. Ow-Yang, M. Sahin, S. Nizamoglu, *Sci. Rep.* **2021**, 11, 2460.
- [21] R. Melikov, S. B. Srivastava, O. Karatum, I. B. Dogru-Yuksel, U. M. Dikbas, I. H. Kavakli, S. Nizamoglu, *Biomed. Opt. Express* **2020**, 11, 6068.
- [22] T. Flores, G. Goetz, X. Lei, D. Palanker, *J. Neural Eng.* **2016**, 13, 036010.
- [23] a) K. Melzer, M. Brändlein, B. Popescu, D. Popescu, P. Lugli, G. Scarpa, *Faraday Discuss.* **2014**, 174, 399; b) T. Cramer, A. Kyndiah, M. Murgia, F. Leonardi, S. Casalini, F. Biscarini, *Appl. Phys. Lett.* **2012**, 100, 143302; c) R. Melikov, S. B. Srivastava, O. Karatum, I. B. Dogru-Yuksel, H. Bahmani Jalali, S. Sadeghi, U. M. Dikbas, B. Ulgut, I. H. Kavakli, A. E. Cetin, *ACS Appl. Mater. Interfaces* **2020**, 12, 35940.
- [24] O. Karatum, M. M. Aria, G. O. Eren, E. Yildiz, R. Melikov, S. B. Srivastava, S. Surme, I. B. Dogru, H. Bahmani Jalali, B. Ulgut, *Front. Neurosci.* **2021**, 15, 724.
- [25] W. A. Rutala, M. F. Gergen, D. J. Weber, *Am. J. Infect. Control* **1998**, 26, 393.
- [26] T. K. Lim, B. A. MacLeod, C. R. Ries, S. K. Schwarz, *Anesthesiology* **2007**, 107, 305.
- [27] R. Plonsey, R. C. Barr, *Bioelectricity: A Quantitative Approach*, Springer Science & Business Media, **2007**.
- [28] B. P. Bean, *Nat. Rev. Neurosci.* **2007**, 8, 451.
- [29] R. Parameswaran, J. L. Carvalho-de-Souza, Y. Jiang, M. J. Burke, J. F. Zimmerman, K. Koehler, A. W. Phillips, J. Yi, E. J. Adams, F. Bezanilla, *Nat. Nanotechnol.* **2018**, 13, 260.
- [30] O. S. Abdullaeva, F. Balzer, M. Schulz, J. Parisi, A. Lützen, K. Dedek, M. Schiek, *Adv. Funct. Mat.* **2019**, 29, 1805177.
- [31] J. D. Loudin, S. F. Cogan, K. Mathieson, A. Sher, D. V. Palanker, *IEEE Trans. Biomed. Circuits Syst.* **2011**, 5, 468.